Supporting Information

Assessment of strain-generated oxygen vacancies via $SrTiO_3$ bicrystals

Si-Young Choi, Sung-Dae Kim, Minseok Choi*, Hak-Sung Lee, Jungho Ryu, Teruyasu Mizoguchi, Naoya Shibata, Eita Tochigi, Takahisa Yamamoto, Suk-Joong L. Kang, and Yuichi Ikuhara*

Details of Methods

***Sample preparation*:** [001] symmetric tilt boundaries with tilt angles of 6° and 10° were prepared by joining two single crystals. Commercial STO single crystals doped with 0.2 at.% Nb (Earth Chemical Co. Ltd) were used. The size of the single crystals was 10 × 10 × 3 mm with the {100} surface plane. The broad face of 10 × 10 mm inclined at half of the tilt angle from (010) was applied as a contacting plane. The contacting planes of the single crystals were ground and polished to a mirror finish with a 0.25-μm diamond slurry. Subsequently, two single crystals were stacked to adjust the edges of the respective single crystals, and the stacked pair was heated to 1873 K for 10 h in air. The heating and cooling rates were 200 K/h. After the joining was completed, several plates 10 × 10 × 1 mm in size were cut from the bicrystals for I-V measurements and for the TEM sample preparation. After printing Ag-ohmic paste as electrodes at 500°C for 0.5 h, the current–voltage (I–V) relationship was measured with a computerized system consisting of a current source (Keithley, Model 220) and a voltage meter (Keithley, Model 2010) at room temperature. Thin foils were also prepared using the conventional method, which included mechanical thinning to ~20 μm and ion beam milling to electron transparency at an acceleration voltage of 2–4 kV using an Ar ion beam. The grain boundary atomic structures were investigated using a high-resolution TEM (JEOL JEM-4010, JEOL Ltd., Tokyo, Japan) operated at 400 kV and a HAADF STEM (JEOL JEM-2100F, JEOL Ltd., Tokyo, Japan) equipped with an aberration corrector (CEOS GmbH, Heidelberg, Germany). The probe diameter

of the beam was approximately 1 Å. For the HAADF imaging, a probe convergence angle of approximately 22 mrad was used. The inner angles of the HAADF and LAADF detectors were greater than 80 mrad and 30 mrad, respectively.

***Calculation to predict Ti-$L_{2,3}$ and the O-K edge EELS spectra*:** Theoretical calculations of Ti-$L_{2,3}$ and O-*K* edge EELS were performed using the density-functional theory configuration interaction method[S1]. For Ti-$L_{2,3}$ EELS calculation, the inter-electron interactions among the Ti 2*p*, 3*d*, and ligand O 2*p* electrons were explicitly calculated, while the interactions between those electrons and other electrons were considered via local density approximations. For the Slater determinants, O 2*p* was considered as well as the Ti 2*p* and 3*d* orbitals. The calculation was performed with seven atom clusters embedded in the Madelung potential of STO. For the Ti^{3+} calculation (Figure S3), the same cluster and Madelung potential of STO were used, but the cluster was assumed to include one extra electron. The effect of strain on the spectrum (Figure S5) was considered by expanding and compressing the atomic arrangements in the cluster and the Madelung potential. To calculate O-*K* EELS, the interactions among the O1*s* and 2*p* electrons were calculated by using the core-hole method and the electronic interactions were considered via as local density approximations.

***First-principles defect calculations*:** Our calculations were carried out using the projector augmented-wave method[S2] and the exchange-correlation functional of the generalized-gradient approximation[S3] implemented in the VASP code[48]. For defect simulations, the wavefunctions were expanded in a plane-wave basis set with an energy cutoff of 400 eV, and supercells containing 320 atoms were used with $2 \times 2 \times 2$ k-point sampling. The atomic coordinates were fully relaxed until the force acting on each atom was reduced to less than 0.02 eV/Å. The formation energy of an oxygen vacancy in STO was evaluated as[S4] $E^f(V_O^0) = E_{tot}(V_O^0) -$

$E_{tot}(\mathrm{STO}) + \mu_{\mathrm{O}}$, where $E_{tot}(V_{\mathrm{O}}^{0})$ is the total energy of a supercell containing a neutral oxygen vacancy and $E_{tot}(\mathrm{STO})$ is the total energy of a pristine STO supercell. μ_{O} is the oxygen chemical potential. Biaxial strains were imposed by applying smaller (for compressive strain) or larger in-plane lattice constants (for tensile strain) than the equilibrium lattice constant (a_0) in the supercell. Hydrostatic pressure was employed in the same manner by varying all three lattice vectors of cubic STO. Regarding the shear strain, a tilt angle θ is used as a control parameter. The percent of shear strain γ is quantified as $\tan^{-1}(\gamma\ \%) = \tan^{-1}(2\gamma\ /100) = \theta$ (see Figure 6b). To calculate the relative formation energy of oxygen vacancies between strained and unstrained STO, the difference $E^{f}(V_{\mathrm{O}}^{0})$ was taken between the total energy of the supercell under strain and at equilibrium. For instance, under 2% tensile strain ($a = 1.02a_0$), the relative formation energy was estimated by $[E_{tot}(V_{\mathrm{O}}^{0}) - E_{tot}(\mathrm{STO})]@2\%\text{-tensile} - [E_{tot}(V_{\mathrm{O}}^{0}) - E_{tot}(\mathrm{STO})]@\mathrm{equilibrium}$ under the assumption that changes in μ_{O} under strain are negligible.

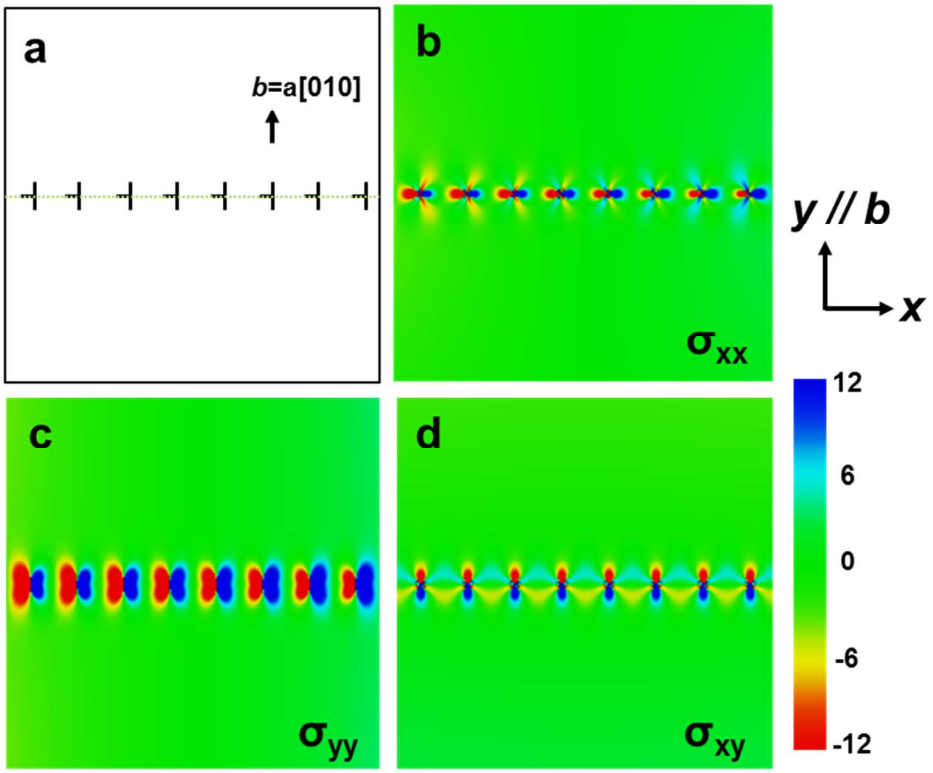

Figure S1. The stress field along (a) an imaginary symmetrical tilt GB (tilt angle of 10 degree) calculated using numerical equations[S5] of the stress components [$\sigma_{yy} = -\frac{Gb}{2\pi(1-\nu)} \cdot x \frac{3y^2+x^2}{(x^2+y^2)^2}$ $\sigma_{xx} = \frac{Gb}{2\pi(1-\nu)} \cdot x \frac{y^2-x^2}{(x^2+y^2)^2}$ $\sigma_{xy} = \sigma_{yx} = \frac{Gb}{2\pi(1-\nu)} \cdot y \frac{y^2-x^2}{(x^2+y^2)^2}$, G (shear modulus of STO)=117GPa [S6], ν (Poisson ratio of bulk STO)=0.232 [S7], *b* (Burgers vector of the dislocations in STO)=**a**[010]] induced by the pure edge dislocations. (b), (c) and (d) are the calculated in-plane stress field distributions of σ_{xx}, σ_{yy}, and σ_{xy}, respectively, around the dislocation cores.

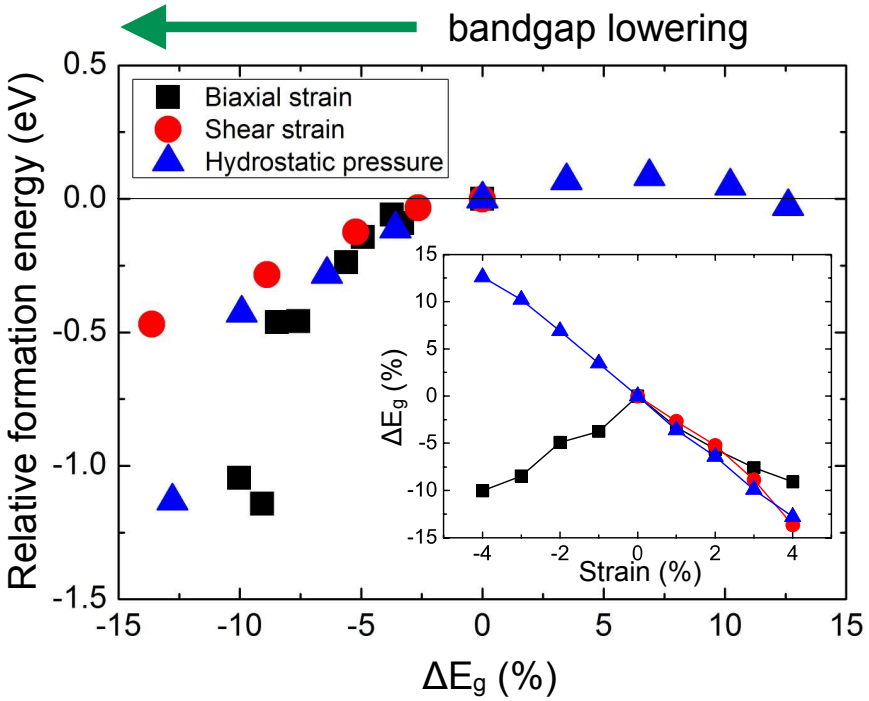

Figure S2: Relative formation energy of oxygen vacancies as a function of the ratio of the calculated band-gap under strains and hydrostatic pressure. Inset: the band-gap changes with the strain are plotted. ΔE_g is defined as $[E_g(\text{strain or pressure})/E_g(\text{equilibrium}) - 1] \times 100$, where E_g (strain or pressure) is the calculated band-gap under strain or pressure, and E_g (equilibrium) is that at equilibrium. All types of strains, such as biaxial tensile, biaxial compressive, and shear strain, give rise to a reduction of the band-gap and accordingly decrease the formation energy of oxygen vacancies. Although hydrostatic compressive pressure widens the band-gap, contrary to the hydrostatic tensile pressure, biaxial tensile, biaxial compressive, and shear strain, the formation energy of oxygen vacancies is not obviously affected by an increased band-gap. On the other hand, the formation energy is more drastically decreased by a decreased band-gap. Herein, our results show the correlation between the formation energy of oxygen vacancies and band-gap changes with various types of strains and pressures acting on a STO crystal.

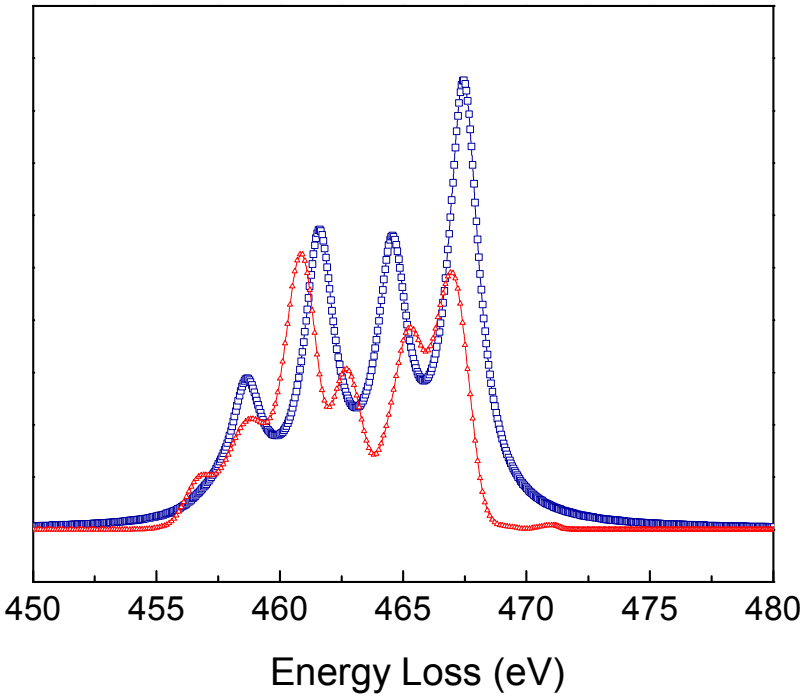

Figure S3. Calculated Ti-*L* edge EELS spectra according to the Ti valence state; +4 (blue) and +3 (red). The Ti-*L* edge shifts to a lower energy level and t_{2g} is annihilated as the valence state changes from +4 to +3. Because t_{2g} at the Ti-*L* edge derives from the strong covalent bonding between the *d*-shell of Ti and the *p*-shell of O, detection of the change in the Ti-*L* edge is useful to identify the Ti valence state directly.

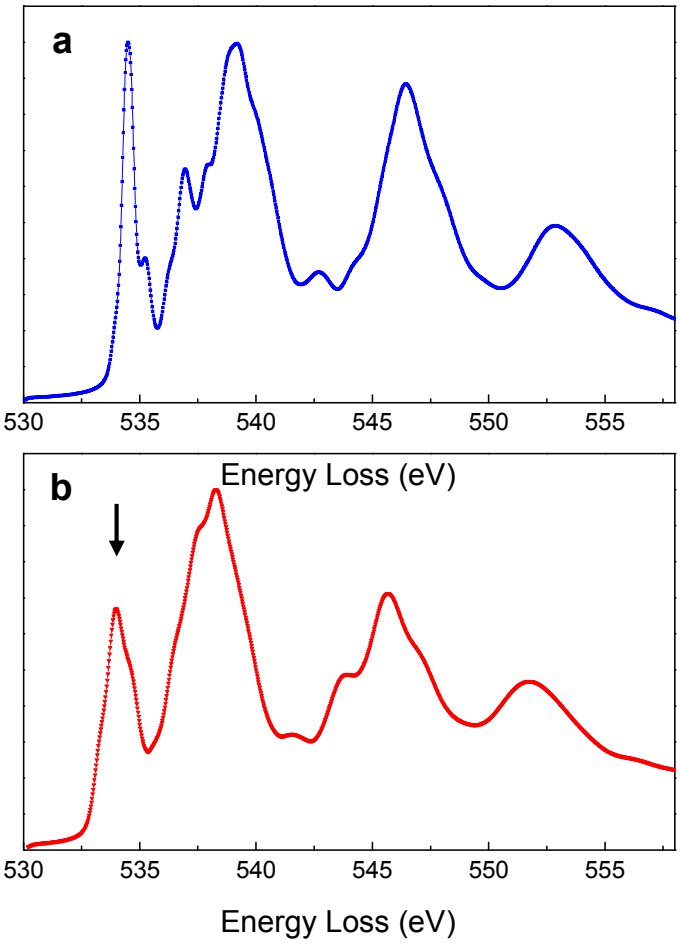

Figure S4: Calculated O-*K* edge EELS spectra of (a) pristine $SrTiO_3$ and (b) $SrTiO_3$ with a positively charged oxygen vacancy. Both calculations were performed with a 3 x 3 x 3 supercell via core hole methods. Suppression of the first peak as indicated by the arrow is related to the Ti valence state and/or the excess electrons occupying the conduction band near the oxygen p-Ti t_{2g} orbital.

References

S1. Ikeno, H.; Mizoguchi, T.; Koyama, Y.; Kumagai, Y.; Tanaka, I. *Ultramicroscopy* **2006,** 106, (11-12), 970-5.

S2. Blöchl, P. E. *Phys. Rev. B* **1994,** 50, 17953.

S3. Perdew, J. P.; Burke, K.; Ernzerhof, M. *Phys. Rev. Lett.* **1996,** 77, 3865.

S4. Kresse, G.; Hafner, J. *Phys. Rev. B* **1993,** 48, 13115

S5. Hull, D.; Bacon, D. J. *Introduction to Dislocations*. 3 edn, (Pergamon Press, 1984).

S6. Bell, R. O.; Rupperchi, G. *Phys. Rev.* **129**, 90-98 (1963).

S7. Ledbetter, H.; Lei, M. ; Kim, S.. *Phase Transitions* **23**, 61-70 (1990).